Exact and Approximate Fourier Rebinning of PET Data from Time-of-Flight to Non Time-of-Flight

Sanghee Cho, **Sangtae Ahn**, **Quanzheng Li**, and **Richard M. Leahy**

Signal and Image Processing Institute, University of Southern California, Los Angeles, CA 90089, USA

Richard M. Leahy: leahy@sipi.usc.edu

Abstract

The image reconstruction problem for fully 3D TOF PET is challenging because of the large data sizes involved. One approach to this problem is to first rebin the data into one of the following lower dimensional formats: 2D TOF, 3D non TOF, or 2D non TOF. Here we present a unified framework based on a generalized projection slice theorem for TOF data that can be used to compute each of these mappings. We use this framework to develop approaches for rebinning into non TOF formats without significant loss of information. We first derive the exact mappings and then describe approximations which address the missing data problem for oblique sinograms. We evaluate the performance of approximate rebinning using Monte Carlo simulations. Our results show that rebinning into non TOF sinograms retains significant SNR advantages over sinograms collected without TOF information.

1. Introduction

Fully 3D time-of-flight (TOF) PET scanners offer the potential for previously unachievable signal to noise ratio in clinical PET. Recent developments of fast scintillators such as LSO (Moses and Derenzo 1999) and LaBr$_3$ (Kuhn et al. 2004) make clinical TOF PET practical (Surti et al. 2006, Surti et al. 2007). However, fully 3D TOF PET image reconstruction using accurate system and noise models is a challenging task due to the huge data size. One approach to this problem is to first rebin 3D TOF PET data into a lower dimensional space. The single slice rebinning (SSRB-TOF) of (Mullani et al. 1982) combines the oblique TOF sinograms to form a set of stacked 2D TOF sinograms in a similar manner to SSRB for non TOF data. As an alternative to SSRB-TOF, Defrise and his colleagues proposed an approximate Fourier rebinning method, where the rebinning is performed in the Fourier domain. This approximate approach shows improved performance over SSRB-TOF (Defrise et al. 2005). An exact rebinning equation was derived based on a consistency condition expressed by a partial differential equation in the continuous data domain (Defrise et al. 2008), where rebinning is performed with respect to the axial variables. This result motivated the development of an approximate discrete axial rebinning method. In this method a cost function based on a bias and variance tradeoff is used to find optimal pre-computable rebinning coefficients. Using these coefficients, a weighted average of the axial lines of response is taken to estimate an appropriate line of response in a 2D direct plane. In our previous paper (Cho et al. 2008), we developed an alternative exact rebinning method which is based on the Fourier transform in the time of flight variable.

All the rebinning methods reviewed above rebin 3D TOF data to 2D TOF data and specifically retain the TOF component in the rebinned data. Here we propose novel rebinning methods that rebin 3D TOF data to non TOF data in either 3D or 2D forms. A generalized projection slice theorem derived in our previous paper (Cho et al. 2008) is used to set up a unified framework to find all possible mappings between different data sets. Figure 1 illustrates all such mappings. Mapping D was used for the original Fourier rebinning methods for non TOF data (Defrise et al. 1997), and mapping B between 3D and 2D TOF data was introduced in (Defrise et al. 2005). Mapping A between 3D TOF data and 3D non TOF data, and mapping C between 3D TOF data and 2D non TOF data are the cases considered in this paper. Mapping E is a special case of mapping A for 2D TOF PET data. Note that the rebinnings A and C use the TOF information as part of the rebinning process so that the result of rebinning is not an explicit function of the timing information. However, since the mappings themselves do make use of the TOF information, the rebinned non TOF data are able to retain SNR advantages relative to count-matched data acquired without TOF information, or equivalently rebinnings computed by simply summing sinograms over the TOF bins.

We first derive exact mapping equations for rebinning 3D TOF data to 3D or 2D non TOF data. Both equations require a Fourier transform in the axial direction. However, the oblique data are axially truncated due to the finite axial aperture of the scanner. To address the missing data problem, we apply approximate mapping equations as in (Defrise et al. 1997). Next we evaluate the proposed rebinning methods. First, we investigate the accuracy of the approximate rebinning methods. Then we conduct Monte Carlo simulations to examine the noise properties of the rebinnings. Finally, we perform 3D TOF PET reconstruction from noisy data using the rebinning methods and compare results with those from using 3D non TOF data.

2. Theory

2.1. Derivation of mapping equations

The 3D TOF PET data p from a cylindrical scanner can be modeled as a line integral weighted by a TOF kernel h (Defrise et al. 2005):

$$p(s,\phi,z,\delta;t)=\sqrt{1+\delta^2}\int_{-\infty}^{\infty}f(s\cos\phi-l\sin\phi,s\sin\phi+l\cos\phi,z+l\delta)h(t-l\sqrt{1+\delta^2})dl \quad (1)$$

where f denotes a 3D object, s and φ are the radial and angular coordinates, respectively, z is the axial midpoint of each line of response (LOR), δ is the tangent of the oblique angle θ, and t is the TOF variable (see figure 2). The TOF kernel is assumed to be shift invariant so that the integral in (1) can be written in the form of a convolution. If $h = 1$, then p in (1) represents non TOF data. When $\delta = 0$, p represents stacked 2D sinograms; in this paper the stacked 2D sinograms are simply referred to as 2D data.

From (1), the following equation representing the generalized projection slice theorem for 3D TOF PET data can be derived in a cylindrical scanner geometry (Cho et al. 2008):

$$\wp(\omega_s, \phi, \omega_z, \delta; \omega_t) = \sqrt{1+\delta^2} H(\omega_t) F(\omega_s\cos\phi - \chi\sin\phi, \omega_s\sin\phi + \chi\cos\phi, \omega_z) \quad (2)$$

where F and H are the Fourier transforms of f and h, respectively; $\wp$ is the Fourier transform of $p(s, \varphi, z, \delta; t)$ with respect to s, z and t; ω_s, ω_z and ω_t are the frequency variables corresponding to s, z and t, and

$$\chi = \omega_t\sqrt{1+\delta^2} - \delta\omega_z. \quad (3)$$

The relationship in (2) also applies to other cases: a 3D non TOF PET case (when $\omega_t = 0$), a 2D TOF case (when $\delta = 0$) and a 2D non TOF case (when $\omega_t = 0$ and $\delta = 0$). Note that $\omega_t = 0$ corresponds to the DC component in the TOF variable direction, which is the sum through the TOF bin variable t and therefore represents non TOF data (Cho et al. 2008). This theorem may also be used as the basis for direct Fourier reconstruction from TOF data in a similar manner to the Fourier-based image reconstruction in (Matej and Kazantsev 2006) for 3D non TOF PET.

The generalized projection slice theorem in (2) enables us to find exact mappings between various data sets. For example, a mapping between 3D TOF data and 3D non TOF data can be obtained as follows. First, by setting ω_t to zero we have:

$$\wp(\omega_s, \phi, \omega_z, \delta; 0) = \sqrt{1+\delta^2} H(0) F(\omega_s\cos\phi + \delta\omega_z\sin\phi, \omega_s\sin\phi - \delta\omega_z\cos\phi, \omega_z). \quad (4)$$

This relationship was originally used to derive the exact Fourier rebinning (FOREX) equation in (Liu et al. 1999). Equating the right hand sides of (2) and (4), we then have the following result:

$$\wp(\omega_s, \phi, \omega_z, \delta; \omega_t) = \{H(\omega_t)/H(0)\}\wp(\omega_s', \phi', \omega_z, \delta; 0) \quad (5)$$

subject to the following relationships:

$$\omega_x = \omega_s\cos\phi - \chi\sin\phi = \omega_s'\cos\phi' + \delta\omega_z\sin\phi' \\ \omega_y = \omega_s\sin\phi + \chi\cos\phi = \omega_s'\sin\phi' - \delta\omega_z\cos\phi' \quad (6)$$

with ω_x and ω_y denoting the first two coordinates of F. By solving (6) for ω_s' and ϕ', we then obtain an exact inverse rebinning mapping from 3D non TOF data to 3D TOF data:

$$\omega_s' = \omega_s\sqrt{1 + \frac{\chi^2 - (\delta\omega_z)^2}{\omega_s^2}} \\ \phi' = \phi + \arctan\left(\frac{\chi}{\omega_s}\right) + \arctan\left(\frac{\delta\omega_z}{\omega_s}\right). \quad (7)$$

In a similar manner one can derive each of the other mappings listed in table 1 using the generalized projection slice theorem (2). Mapping D is equivalent to exact inverse Fourier rebinning (Defrise et al. 1997) and the exact Fourier rebinning equation (Liu et al. 1999) that maps between 2D non TOF data and 3D non TOF data. In (Cho et al. 2008), we used

mapping C to derive the exact inverse rebinning mapping from 2D non TOF data to 3D TOF data and used mapping B to derive the exact rebinning mapping from 3D TOF data to 2D TOF data. Mapping A, from which (7) is derived, and its 2D version, mapping E, are the main new results presented in this paper.

2.2. Non TOF Fourier rebinning and approximation (mapping D)

Since the approximate TOF rebinning methods described below use similar approximations to those for the non TOF case, we first review the exact and approximate Fourier rebinning for non TOF data (Defrise 1995, Defrise et al. 1997). The exact inverse Fourier rebinning equation (Defrise et al. 1997) can be written as

$$\wp(\omega_s, \phi, \omega_z, \delta; 0) = \sqrt{1+\delta^2} \, \wp\left(\omega_s\sqrt{1+\left(\frac{\delta\omega_z}{\omega_s}\right)^2}, \phi - \arctan\left(\frac{\delta\omega_z}{\omega_s}\right), \omega_z, 0; 0\right), \quad (8)$$

which can be derived from Mapping D in table 1. Note that the original form presented in (Defrise et al. 1997) can be obtained by taking the Fourier transform of (8) with respect to φ. Figure 3 shows a graphical interpretation of the exact mapping (8) in the (ω_x, ω_y) plane for fixed ω_z in the image Fourier domain. The projection slice theorem relates 3D data to 2D data through the (ω_x, ω_y) plane for each ω_z. In Figure 3, the line joining the points A and B is a trajectory (ω_x, ω_y) corresponding to 3D non TOF PET data $\wp(\omega_s, \varphi, \omega_z, \delta; 0)$ parameterized by ω_s for fixed φ, ω_z and δ, through the relationships $\omega_x = \omega_s \cos\varphi + \delta\omega_z \sin\varphi$ and $\omega_y = \omega_s \sin\varphi - \delta\omega_z \cos\varphi$, as given in mapping D in table 1. Then, exact inverse Fourier rebinning finds the coordinates (ω_s', ϕ') of (ω_x, ω_y) (for example, point B in Figure 3) through the relationships $\omega_x = \omega_s'\cos\phi'$ and $\omega_y = \omega_s'\sin\phi'$ for 2D non TOF data $\wp(\omega_s', \phi', \omega_z, 0; 0)$.

The exact mapping equation requires the Fourier transform of the data in the z direction. However, the oblique sinograms in 3D PET data are not axially complete since the data are truncated due to the finite axial aperture of the scanner. One needs to estimate the missing data before applying the rebinning (Liu et al. 1999). Alternatively, one can use the first order Taylor series truncation with respect to $\delta\omega_z/\omega_s$,

$$\omega_s' = \omega_s\sqrt{1+\left(\frac{\delta\omega_z}{\omega_s}\right)^2} \approx \omega_s, \quad \phi' = \phi - \arctan\left(\frac{\delta\omega_z}{\omega_s}\right) \approx \phi - \frac{\delta\omega_z}{\omega_s}, \quad (9)$$

to obtain an approximation to (8):

$$\wp(\omega_s, \phi, \omega_z, \delta; 0) \approx \sqrt{1+\delta^2}\,\wp\left(\omega_s, \phi - \frac{\delta\omega_z}{\omega_s}, \omega_z, 0; 0\right). \quad (10)$$

By taking the Fourier transform of (10) in φ and then taking the inverse Fourier transform in ω_z and using the shift property of Fourier transforms, one can obtain the Fourier rebinning (FORE) equation (Defrise 1995, Defrise et al. 1997)

$$\mathscr{P}(\omega_s, k, z, \delta; 0) \approx \sqrt{1+\delta^2}\,\mathscr{P}\left(\omega_s, k, z-\frac{\delta k}{\omega_s}, 0; 0\right) \quad (11)$$

where k is the Fourier series index corresponding to φ and $\mathscr{P}$ is the 3D Fourier transform of $p(s, \varphi, z, \delta; t)$ in s, φ and t. Note that (11) does not require the Fourier transform in the z direction. The approximation in (9) becomes more inaccurate as $|\delta\omega_z/\omega_s|$ increases. To reduce approximation errors, Defrise *et al.* used only oblique sinograms for small δ when $|\omega_s|$ is small (Defrise et al. 1997).

2.3. TOF rebinning mappings and approximations

We now consider mappings A and C in table 1, which rebin 3D TOF data to 3D and 2D non TOF data, respectively. To address the missing data problem, we propose approximations similar to the non TOF case reviewed in section 2.2 above, which do not require the Fourier transform in z. The Fourier rebinnings using mappings A and C are called FORET-3D (FOurier REbinning of Time-of-flight data to 3D non time-of-flight) and FORET-2D (FORET to 2D non time-of-flight), respectively.

2.3.1. Approximate mapping between 3D TOF and 2D non TOF data (mapping C)—Noting that the mapping equations for mapping C in table 1 are the same as those for mapping D for non TOF data except for the $-\omega_z$ and χ terms, we use a first order Taylor series truncation with respect to χ/ω_s, similar to (9),

$$\omega_s' = \omega_s\sqrt{1+\left(\frac{\chi}{\omega_s}\right)^2} \approx \omega_s \triangleq \tilde{\omega}_s', \quad \phi' = \phi + \arctan\left(\frac{\chi}{\omega_s}\right) \approx \phi + \frac{\chi}{\omega_s} \triangleq \tilde{\phi}'. \quad (12)$$

Note that $\chi/\omega_s = (\omega_t\sqrt{1+\delta^2}-\delta\omega_z)/\omega_s$ is reasonably small as long as ω_s is not too small for the following reasons. First, $\delta\omega_z/\omega_s$ is sufficiently small, as assumed when deriving the FORE equation in (11), since δ is practically small. Second, ω_t is small compared to ω_s in practice because the sampling interval in s is much smaller than that in the t direction. For example, in the realistic 3D TOF PET scanner simulated in section 3, the fold-over frequencies for t and s were $\omega_t^{\text{fold-over}} = \pi/\Delta t = \pi/(37.9\text{mm}) = 0.0829\,\text{rad/mm}$ and $\omega_s^{\text{fold-over}} = \pi/\Delta s = \pi/(1.9682\text{mm}) = 1.5962\,\text{rad/mm}$, respectively. This difference arises naturally from the relatively low resolution in the TOF direction compared to spatial sampling of the sinogram determined by the detector spacing.

The approximation in (12) leads to the following approximate inverse rebinning equation

$$\wp(\omega_s, \phi, \omega_z, \delta; \omega_t) \approx \{H(\omega_t)/H(0)\}\wp\left(\omega_s, \phi + \frac{\omega_t\sqrt{1+\delta^2}-\delta\omega_z}{\omega_s}, \omega_z, 0; 0\right). \quad (13)$$

By taking the Fourier transform in φ and then taking the inverse Fourier transform in ω_z and using the shift property of Fourier transforms, one can rewrite (13) as

$$\mathscr{P}(\omega_s, k, z, \delta; \omega_t) \approx \sqrt{1+\delta^2}\{H(\omega_t)/H(0)\}e^{ik\left(\frac{\omega_t\sqrt{1+\delta^2}}{\omega_s}\right)}\mathscr{P}\left(\omega_s, k, z-\frac{\delta k}{\omega_s}, 0;0\right), \quad (14)$$

which does not require a Fourier transform in the z direction. Similarly, an approximate rebinning equation can be written as

$$\mathscr{P}(\omega_s, k, z, 0;0) \approx \frac{1}{\sqrt{1+\delta^2}}\{H(0)/H(\omega_t)\}e^{-ik\left(\frac{\omega_t\sqrt{1+\delta^2}}{\omega_s}\right)}\mathscr{P}\left(\omega_s, k, z+\frac{\delta k}{\omega_s}, \delta;\omega_t\right), \quad (15)$$

which is used for FORET-2D. Figure 3 also applies to this case if we use χ in place of $-\delta\omega_z$. Considering that (14) and the FORE equation (11) are of the same form except the scaling term $\{H(\omega_t)/H(0)\}\exp(ik\omega_t\sqrt{1+\delta^2}/\omega_s)$, one can implement FORET-2D using the existing FORE code with minor modifications. The errors due to the approximations in (12) are comparable to those from (9) for FORE, as we show in section 2.3.3.

2.3.2. Approximate mapping between 3D TOF data and 3D non TOF data (mapping A)

—The exact equations mapping between 3D TOF and 3D non TOF data are given in (5) and (7). To remove the dependency on ω_z, we make the following approximation,

$$\begin{aligned}
\omega_s' &= \omega_s\sqrt{1+\frac{\chi^2-(\delta\omega_z)^2}{\omega_s^2}} = \omega_s\sqrt{1+\left(\frac{\omega_t\sqrt{1+\delta^2}}{\omega_s}\right)^2 - 2\left(\frac{\omega_t\sqrt{1+\delta^2}}{\omega_s}\right)\left(\frac{\delta\omega_z}{\omega_s}\right)} \\
&\approx \omega_s\sqrt{1+\left(\omega_t\sqrt{1+\delta^2}/\omega_s\right)^2} \triangleq \tilde{\omega}_s' \\
\phi' &= \phi+\arctan\left(\frac{\omega_t\sqrt{1+\delta^2}-\delta\omega_z}{\omega_s}\right)+\arctan\left(\frac{\delta\omega_z}{\omega_s'}\right) \\
&\approx \phi+\arctan\left(\omega_t\sqrt{1+\delta^2}/\omega_s\right) \triangleq \tilde{\phi}',
\end{aligned} \quad (16)$$

which can be seen as the zeroth order Taylor series truncation with respect to $\delta\omega_z/\omega_s$. This approximation yields the following approximate inverse rebinning equation:

$$P(\omega_s, \phi, z, \delta; \omega_t) \approx \frac{H(\omega_t)}{H(0)}P\left(\omega_s\sqrt{1+\left(\omega_t\sqrt{1+\delta^2}/\omega_s\right)^2}, \phi+\arctan\left(\omega_t\sqrt{1+\delta^2}/\omega_s\right), z, \delta;0\right) \quad (17)$$

where P is the 2D Fourier transform of $p(s, \varphi, z, \delta; t)$ in s and t. The corresponding approximate rebinning equation can be written as

$$P(\omega_s, \phi, z, \delta;0) \approx \frac{H(0)}{H(\omega_t)}P\left(\omega_s\sqrt{1-\left(\omega_t\sqrt{1+\delta^2}/\omega_s\right)^2}, \phi-\arctan\left(\omega_t\sqrt{1+\delta^2}/\omega_s'\right), z, \delta;\omega_t\right), \quad (18)$$

which is used for FORET-3D, where $\omega_s' = \omega_s\sqrt{1-\left(\omega_t\sqrt{1+\delta^2}/\omega_s\right)^2}$.

The approximation error will increase with $|\delta\omega_z/\omega_s|$, and also with $|\omega_t|$ due to the term ($\omega_t \sqrt{1+\delta^2}/\omega_s$) which is ignored when approximating ω_s' in (16). Note that the approximations in (17) and (18) are exact for direct sinograms ($\delta = 0$), and the approximate rebinning method uses fixed δ and z. In other words, the non TOF sinogram for a given (z, δ) is computed only from the TOF data for the same axial plane z with the oblique angle δ.

Figure 4 is a modified version of Figure 3 for this mapping. Here, point B corresponds to the 3D TOF PET data $\wp(\omega_s, \varphi, \omega_z, \delta; \omega_t)$ in the (ω_x, ω_y) plane. The inverse rebinning is equivalent to finding the 3D non TOF data $\wp(\omega_s', \phi', \omega_z, \delta; 0)$ where ω_s' denotes the line segment from point C to B and ϕ' is the sum of φ and $\angle ABC$. The approximation in (16) is to take point D in place of point C in Figure 4. That is, ω_s' and ϕ' are approximated by the coordinate information ($|DB|$ and α_{approx}) of the line segment from point D to B.

2.3.3. Comparison of approximation errors—We have described two approximate rebinning mappings (14) and (17). The inverse rebinning equations are used to estimate at each frequency the 3D TOF data $\wp(\omega_s, \varphi, z, \delta; \omega_t)$ from 2D non TOF data $\wp(\omega_s, \varphi, z, 0; 0)$ or 3D non TOF data $\wp(\omega_s, \varphi, z, \delta; 0)$. To quantify the errors from the approximations in (12) and (16), we calculated the Euclidean distance between the exact and approximate points used for estimating the $\wp(\omega_s, \varphi, \omega_z, \delta; \omega_t)$ data in the (ω_x, ω_y) plane as shown in Figure 3 and Figure 4. The error measure is defined as

$$E= \sqrt{\left(\omega_x^{exact}-\omega_x^{approx}\right)^2+\left(\omega_y^{exact}-\omega_y^{approx}\right)^2} \quad (19)$$

where $\omega_x^{exact}, \omega_y^{exact}, \omega_x^{approx}$ and ω_y^{approx} are defined in table 2 for the mappings C and A. For mapping C, after some manipulation, one can obtain

$$E^2=2\omega_s^2+\chi^2-2\sqrt{\omega_s^2+\chi^2}\cos\left(\arctan\left(\frac{\chi}{\omega_s}\right)-\frac{\chi}{\omega_s}\right),$$

which is not a function of φ. Similarly, one can show that the error measure E for mapping A does not depend on φ.

Figure 5 shows the approximation errors averaged over ω_z and ω_t at four different ring differences as a function of transaxial radial frequency ω_s. The FORE case (mapping D) is also included in the figure for comparison. All the approximate mappings tend to have larger errors as the oblique angle (arctan δ) increases. The figure shows that the approximation errors are large when ω_s is small. Therefore, as in the FORE implementation, special treatment is required for small ω_s, as described in the next section.

The approximation errors for the FORET-2D case (mapping C) are similar to those for the FORE case (mapping D) particularly for large ring differences as shown in Figure 5. Observing that

$$\frac{\chi}{-\delta\omega_z} = 1 - \frac{\omega_t\sqrt{1+\delta^2}}{\delta\omega_z} \approx 1 - \frac{\omega_t}{\delta\omega_z}$$

since $\delta \ll 1$, one can see that as the ring difference δ increases, χ approaches $-\delta\omega_z$ and therefore the mapping equations in (12) for FORET-2D become those in (9) for FORE.

As shown in Figure 5, the FORE case (mapping D) has smaller errors than the other approximate mappings when the ring difference is small; however, as the ring difference increases, the FORET-3D case (mapping A) yields smaller errors than the other mappings. This observation can be partially explained as follows. We focus on approximation errors in the radial frequency direction (ω_s'). For mapping A, we define an approximation error as

$$\varepsilon_A \triangleq \left|\left(\omega_s'\right)^2 - \left(\tilde{\omega}_s'\right)^2\right| = 2\left(\frac{\omega_t\sqrt{1+\delta^2}}{\omega_s}\right)\left(\frac{\delta\omega_z}{\omega_s}\right) \approx \frac{2\omega_t\omega_z\delta}{\omega_s^2}$$

since $\delta \ll 1$ where ω_s' and $\tilde{\omega}_s'$ are defined in (16). Similarly, we define an approximation error for mapping D in (9) as

$$\varepsilon_D \triangleq \left|\left(\omega_s'\right)^2 - \omega_s^2\right| = \frac{\omega_z^2\delta^2}{\omega_s^2}$$

Since $\varepsilon_D/\varepsilon_A \approx (\omega_z/(2\omega_t))\delta$, the approximation error ε_D in the radial direction for FORE is smaller than ε_A for FORET-3D when the ring difference δ is small, and ε_D is larger than ε_A for large δ. However, here we do not intend to put much emphasis on the contrast of the approximate mappings regarding approximation errors since for small ω_s modified procedures are taken to avoid excessive errors as described in section 3.1 and both FORET-2D and FORET-3D result in negligible bias as shown in the next section.

3. Results

3.1. Simulation setup

We performed simulation studies in the geometry of the Siemens Biograph PET/CT True Point TrueV scanner (Jakoby et al. 2006), a state-of-the-art clinical scanner with planned TOF capabilities. The scanner geometry and simulation parameters are shown in table 3. A Gaussian TOF kernel function was used for TOF data generation and 3D projections computed based on line integrals as in (Groiselle and Glick 2004). A TOF resolution of 500 ps was used and the data were sampled with the sampling period of 250 ps, leading to 13 TOF bins over the field of view. The NCAT torso phantom as shown in Figure 6 was used as a 3D object (Segars 2001). Attenuation, randoms, scatters and detector efficiencies were not considered.

In FORET-3D, for each ω_t, we estimate 3D non TOF data $\wp(\omega_s, \varphi, z, \delta; 0)$ from the 3D TOF data using the rebinning equation (18) and calculate an average over all ω_t's. As discussed in section 2.3.2, the approximation error is large when $|\omega_s|$ is small and $|\omega_t|$ is large. To reduce such errors as in (Defrise et al. 1997), when $|\omega_s|$ is less than a threshold S_{TH}, we only use the data $\wp(\omega_s, \varphi, z, \delta; \omega_t)$ for $|\omega_t|$ smaller than a threshold T_{TH}. In our simulation, $S_{TH} = 7$ and $T_{TH} = 1$ were used.

For FORET-2D, as mentioned in section 2.3.1, we apply the FORE code with a minor modification to estimate for each ω_t the 2D data $\wp(\omega_s, k, z, 0; 0)$ from the 3D TOF data $\wp(\omega_s, k, z, \delta; \omega_t)$ and then calculate an average over all ω_t's. As suggested in (Defrise et al. 1997), when ω_s and k are less than or equal to ω_{lim} and k_{lim}, respectively, we use only sinograms with oblique angle indices less than δ_{lim}. In our simulation, $\omega_{lim} = 2$, $k_{lim} = 2$ and $\delta_{lim} = 2$ were used.

3.2. Comparison of rebinned data and non TOF data

To evaluate the performance of the approximate rebinning algorithms, we compare rebinned and non TOF sinogram data by Monte Carlo simulation. For comparison studies, we generated 100 noisy 3D TOF sinograms contaminated with Poisson noise, each of which had a total of 20M counts.

First, to evaluate the performance of FORET-3D, we compared 1) rebinned 3D sinograms obtained using FORET-3D from the TOF data and 2) non TOF 3D sinograms obtained by summing the 3D TOF data in the TOF bin direction. The mean and variance of the rebinned data and non TOF data were calculated and compared. Results for planes at axial center for two different ring differences are shown in Figure 7. Figure 7(a) shows the mean of the rebinned sinogram at zero ring difference. Since the approximate rebinning is exact when the ring difference is zero, it is unbiased. Figure 7(c) shows the profiles of the mean for the maximum ring difference. Even at this maximum ring difference there appears to be no significant approximation error. Figure 7(b) and (d) show the profiles of the variance of the rebinned and non TOF sinograms at two different ring differences. As the figures show, significant variance reduction was achieved by the rebinning when compared to simply summing over the TOF bins. This is a perhaps surprising result, since each non TOF sinogram for a fixed (z, δ) is computed from the same data for the two methods compared in these figures: in one case, by summing over the TOF bins, in the other by rebinning using FORET-3D in (18). In both cases the same number of TOF bin samples are summed and rebinned to each non TOF oblique sinogram.

Next, to evaluate the performance of FORET-2D, we compared 2D sinograms for the following three cases. First, we rebinned the 3D TOF to 3D non TOF data by FORET-3D and then rebinned the 3D non TOF to 2D non TOF data by FORE. Second, we rebinned the 3D TOF directly to 2D non TOF by FORET-2D. Third, we rebinned 3D non TOF data, obtained by summing the 3D TOF data in the TOF bin direction, to 2D non TOF data by FORE. The profiles of the mean and variance of a 2D direct sinogram at axial center for those three cases are shown in Figure 8. The mean profiles were nearly the same as shown in Figure 8(a), implying that the rebinning methods such as FORET-2D and FORET-3D do not have significant approximation errors. Figure 8(b) shows that the variance was substantially

reduced by the rebinning methods, FORET-2D and FORET-3D + FORE. The FORE-3D + FORE combination showed slightly lower variance than FORE-2D; however, it will need further investigation to determine whether FORET-2D or FORET-3D performs better in general.

3.3. Comparison of reconstructed images

3.3.1. Monte Carlo simulation for 2D data reconstruction—To conclude we compare reconstructed images from non TOF data, TOF data rebinned to non TOF by FORET-3D, and unrebinned TOF data. For the Monte Carlo (MC) study, we first consider the 2D case. We generated 100 noisy 3D TOF sinograms and used the central plane of the stacked 2D sinograms (zero ring difference) for 2D image reconstruction. The photon count for the central direct 2D sinogram amounted to 1M. Images were reconstructed by the MAP method (Qi et al. 1998). Three cases were compared. First, the noisy TOF data were used for TOF MAP reconstruction (denoted by 'TOF'). Second, we rebinned the TOF data to non TOF data using FORET-3D to rebin the 2D TOF sinogram and then used the rebinned data for MAP reconstruction (denoted by 'FORET-3D'). Lastly, the noisy TOF data was summed over the TOF bins to generate non TOF data and then used for MAP reconstruction (denoted by 'non TOF').

To quantify the resolution and noise properties of the reconstructed images, we calculated the full-width-at-half-maximum (FWHM) of the local impulse response (Fessler and Rogers 1996) and the sample variance of noisy reconstructed images for different regularization parameters. Figure 9 shows the results at 4 different pixel locations (see Figure 6). The results show that FORET-3D gives a better resolution vs. noise trade-off compared to the non TOF case and its performance is somewhat worse than that for the TOF case. Here, the MAP reconstruction method assumed a Poisson model although in practice the Poisson statistics are destroyed by rebinning as discussed in (Comtat et al. 1998, Liu et al. 2001). Despite possible degradation of image qualities due to the incorrect Poisson noise model, FORET-3D showed better performance than the non TOF case where the correct Poisson noise model was employed. We expect that reconstruction using more accurate statistical models will enhance the performance for rebinned data.

3.3.2. Monte Carlo simulation for 3D data reconstruction—Next we conducted a Monte Carlo simulation study for 3D image reconstruction. We generated 100 noisy 3D TOF sinograms with a total of 20M counts. A fully 3D MAP reconstruction method (Qi et al. 1998) was applied to the TOF data rebinned by FORET-3D and also to non TOF data obtained by summing the TOF data in the TOF bin direction. We did not include 3D TOF data reconstruction here due to the high computational cost.

As Figure 10 shows, again FORET-3D yields a better resolution-noise trade-off compared to the non TOF case. Figure 11 shows noisy reconstructed images from rebinned data and non TOF data, with matched resolution of FWHM 3.4mm in the transverse plane. As the figures shows, the 3D MAP reconstruction with the approximate rebinning yields less noisy images compared to the non TOF 3D reconstruction case.

4. Conclusion

Using a generalized projection slice theorem we have developed a unified framework for rebinning of TOF data. Compared to previous rebinning methods (Mullani et al. 1982, Defrise et al. 2005, Vandenberghe et al. 2006, Defrise et al. 2008), where 3D TOF data is rebinned to 2D TOF data, our rebinning methods rebin the 3D TOF data to either 3D or 2D non TOF data. We have also described approximations that allow practical rebinning of TOF to non TOF data. Using simulated data we evaluated the performance of the approximate rebinnings. Both approximate rebinnings from 3D TOF data to 3D non TOF data and to 2D non TOF data were nearly bias-free. But FORET-3D, rebinning 3D TOF to 3D non TOF data, showed slightly less variance than FORET-2D, rebinning 3D TOF to 2D non TOF data in a simulation study. Although fully 3D PET data reconstruction is computationally more demanding than 2D reconstruction applied to rebinned data, fast projectors (Matej et al. 2004, De Man and Basu 2004, Cho et al. 2007, Hong et al. 2007) or dedicated hardware (Shattuck et al. 2002, Bai and Smith 2006, Pratx et al. 2006) significantly reduce the cost and fully 3D iterative reconstruction is now practical in clinical scanners. However, further investigation will be needed for extensive comparisons of FORET-3D and FORET-2D.

Monte Carlo simulations showed that the approximate rebinning method produced improved SNR compared to data without TOF information, but with some loss in performance relative to full use of the TOF data without rebinning. Our proposed methods rebinning to non TOF data formats preserve the advantage of TOF information since they exploit the timing information in the rebinning process whereas the brute force mapping by summing over TOF bins lose all the TOF information completely. Simply summing over TOF bins is equivalent to throwing out all non-DC components of the signal in the TOF frequency ω_t domain while the proposed methods rebin TOF data separately for each frequency ω_t, enabling us to make use of the timing information. We plan to investigate quantitatively the performance of the proposed rebinnings by information theoretic analysis.

We also plan to investigate the degree to which iterative methods optimized for the statistical properties of rebinned data can achieve performance closer to that for the non rebinned case. First, we can optimize image reconstruction methods from rebinned data. We used the MAP reconstruction based on an independent Poisson noise model in our simulation although the rebinned data are correlated and do not follow the Poisson distribution (Comtat et al. 1998, Liu et al. 2001). Using a correct noise model for reconstruction will possibly improve the noise properties in reconstructed images in view of the Gauss-Markov theorem (Lehmann and Casella 1998). Challenges here are estimating the noise covariance of the rebinned data and incorporating the correlated noise covariance into the reconstruction procedure. Second, we can implement fully 3D TOF data reconstruction to examine the best performance achievable from TOF data. Since 3D TOF data follows an independent Poisson noise model, full TOF data reconstruction only requires an extension of the conventional MAP reconstruction for non TOF data. The challenge in this case is to find efficient ways of performing forward and backproject to minimize the computational cost. In closing we note that since 3D TOF data are highly redundant in terms of data sufficiency

conditions, there are a wide range of possible rebinning operators and other optimized methods may be found which achieve superior SNR.

Acknowledgments

References

Bai B, Smith AM. Fast 3D iterative reconstruction of PET images using PC graphics hardware. Proc IEEE Nuclear Science Symp Medical Imaging Conf. 2006:2787–90.

Cho S, Ahn S, Li Q, Leahy LM. Analytical properties of time-of-flight PET data. Phys Med Biol. 2008; 53:2809–21. [PubMed: 18460746]

Cho S, Li Q, Ahn S, Bai B, Leahy RM. Iterative image reconstruction using inverse Fourier rebinning for fully 3-D PET. IEEE Trans Med Imag. 2007; 26(5):745–56.

Comtat C, Kinahan PE, Defrise M, Michel C, Townsend DW. Fast reconstruction of 3D PET data with accurate statistical modeling. IEEE Trans Nucl Sci. 1998; 45(3):1083–9.

De Man B, Basu S. Distance-driven projection and backprojection in three dimensions. Phys Med Biol. 2004; 49:2463–75. [PubMed: 15248590]

Defrise M. A factorization method for the 3-D X-ray transform. Inverse Prob. 1995; 11:983–94.

Defrise M, Casey ME, Michel C, Conti M. Fourier rebinning of time-of-flight PET data. Phys Med Biol. 2005; 50:2749–63. [PubMed: 15930600]

Defrise M, Kinahan PE, Townsend DW, Michel C, Sibomana M, Newport DF. Exact and approximate rebinning algorithms for 3-D PET data. IEEE Trans Med Imag. 1997; 16:145–58.

Defrise M, Panin V, Michel C, Casey ME. Continuous and discrete data rebinning in time-of-flight PET. IEEE Trans Med Imag. 2008; 27:1310–22.

Fessler JA, Rogers WL. Spatial resolution properties of penalized-likelihood image reconstruction methods: Space-invariant tomographs. IEEE Trans Image Processing. 1996; 5(9):1346–1358.

Groiselle CJ, Glick SJ. 3D PET list-mode iterative reconstruction using time-of-flight information. Proc IEEE Nuclear Science Symp Medical Imaging Conf. 2004:2633–8.

Hong IK, Chung ST, Kim HK, Kim YB, Son YD, Cho ZH. Ultra fast symmetry and SIMD-based projection-backprojection(SSP) algorithm for 3-D PET image reconstruction. IEEE Trans Med Imag. 2007; 26:789–803.

Jakoby BW, Bercier Y, Watson CC, Rappoport V, Young J, Bendriem B, Townsend DW. Physical performance and clinical workflow of a new LSO HI-REZ PET/CT scanner. Proc IEEE Nuclear Science Symp Medical Imaging Conf. 2006:3130–4.

Kuhn A, Surti S, Karp J, Raby P, Shah K, Perkins A, Muehllehner G. Design of a lanthanum bromide detector for time-of-flight PET. IEEE Trans Nucl Sci. 2004; 51:2550–7.

Lehmann, EL.; Casella, G. Theory of point estimation. Springer-Verlag; New York: 1998.

Liu X, Comtat C, Michel C, Kinahan P, Defrise M, Townsend D. Comparison of 3D reconstruction with OSEM and FORE+OSEM for PET. IEEE Trans Med Imag. 2001; 20(8):804–13.

Liu X, Defrise M, Michel C, Sibomana M, Comtat C, Kinahan P, Townsend D. Exact rebinning methods for three-dimensional PET. IEEE Trans Med Imag. 1999; 18(8):657–664.

Matej S, Kazantsev IG. Fourier-based reconstruction for fully 3-D PET: Optimization of interpolation parameters. IEEE Trans Med Imag. 2006; 25:845–54.

Matej S, Fessler JA, Kazantsev IG. Iterative tomographic image reconstruction using Fourier-based forward and back-projectors. IEEE Trans Med Imag. 2004; 23:401–12.

Moses WW, Derenzo SE. Prospects for time-of-flight PET using LSO scintillator. IEEE Trans Nucl Sci. 1999; 46:474–8.

Mullani N, Wong W, Hartz R, Philippe E, Yerian K. Sensitivity improvement of TOFPET by the utilization of the inter-slice coincidence. IEEE Trans Nucl Sci. 1982; 29(1):479–83.

Pratx G, Chinn G, Habte F, Olcott P, Levin C. Fully 3-D list-mode OSEM accelerated by graphics processing units. Proc IEEE Nuclear Science Symp Medical Imaging Conf. 2006:2196–202.

Qi J, Leahy RM, Hsu C, Farquhar TH, Cherry SR. Fully 3D Bayesian image reconstruction for the ECAT EXACT HR+ IEEE Trans Nucl Sci. 1998; 45(3):1096–1103.

Segars, WP. PhD thesis. Univ. of North Carolina; Chpel Hill, NC: 2001. Development and application of the new dynamic nurbs-based cardiac-torso (NCAT) phantom.

Shattuck DW, Rapela J, Asma E, Chatzioannou A, Qi J, Leahy R. Internet2-based 3D PET image reconstruction using a PC cluster. Phys Med Biol. 2002; 47:2785–95. [PubMed: 12200939]

Surti S, Karp JS, Popescu LM, Daube-Witherspoon ME, Werner M. Invesigation of time-of-flight benefit for fully 3-D PET. IEEE Trans Med Imag. 2006; 25:529–38.

Surti S, Kuhn A, Werner ME, Perkins AE, Kolthammer J, Karp JS. Performance of Philips Gemini TF PET/CT scanner with special consideration for its time-of-flight imaging capabilities. J Nuc Med. 2007; 48:471–80.

Vandenberghe S, Daube-Witherspoon ME, Lewitt RM, Karp JS. Fast reconstruction of 3D time-of-flight PET data by axial rebinning and transverse mashing. Phys Med Biol. 2006; 51:1603–21. [PubMed: 16510966]
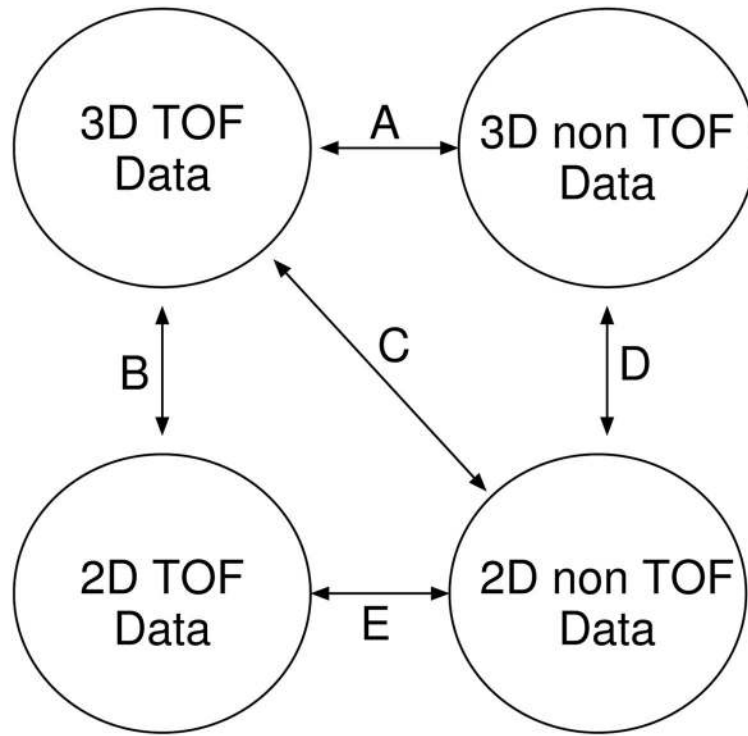
Figure 1.
Using the generalized projection slice theorem, the mappings shown above can be derived.
See table 1 for details.
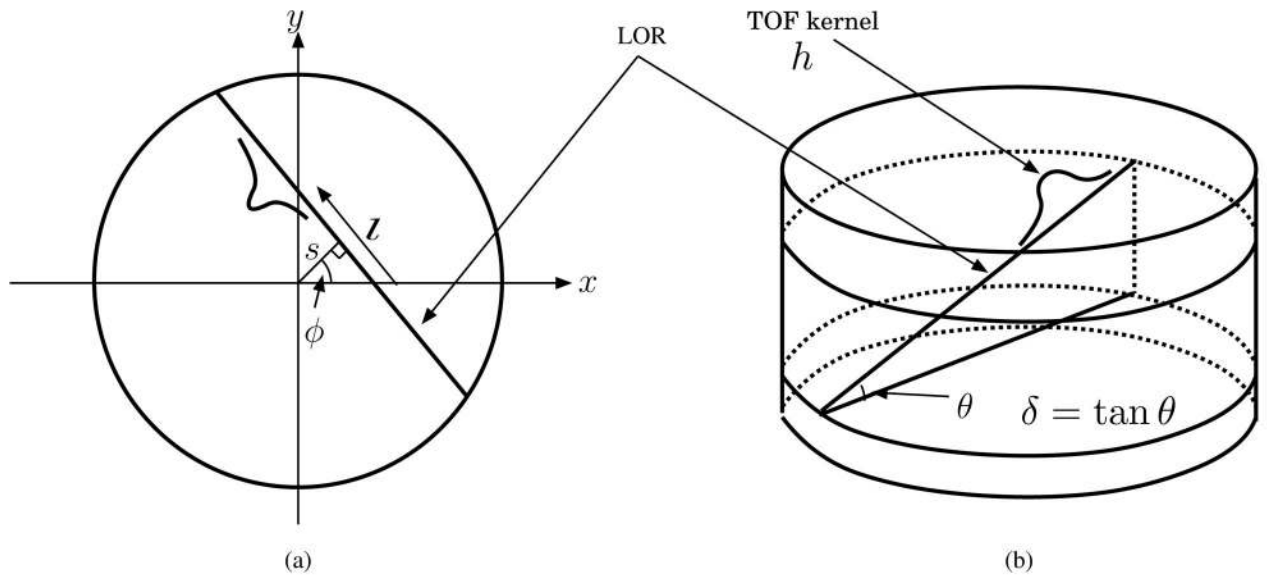
Figure 2.
(a) Transverse and (b) 3D view of a cylindrical 3D PET scanner. For each line of response (LOR), the object is multiplied by the TOF kernel *h* and integrated along the line to form the TOF data.
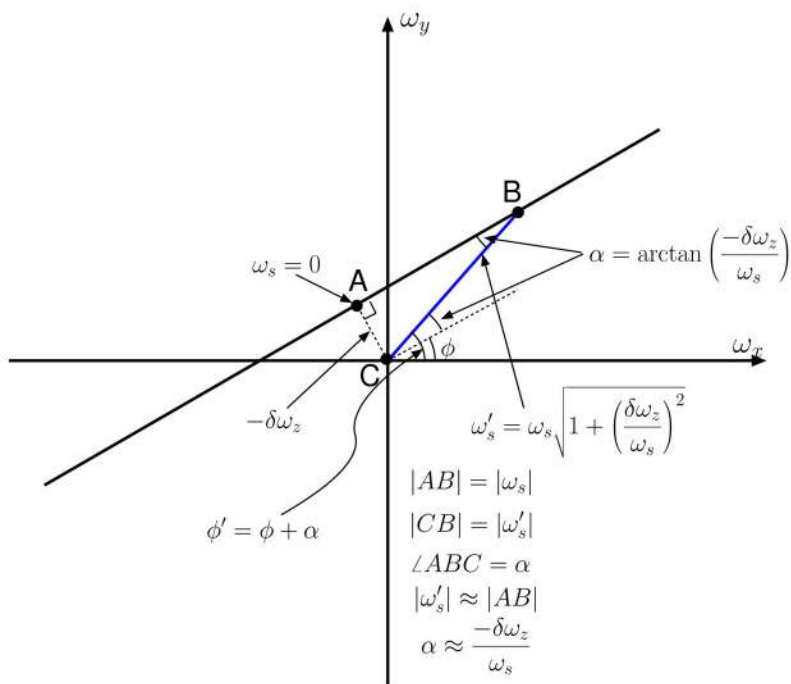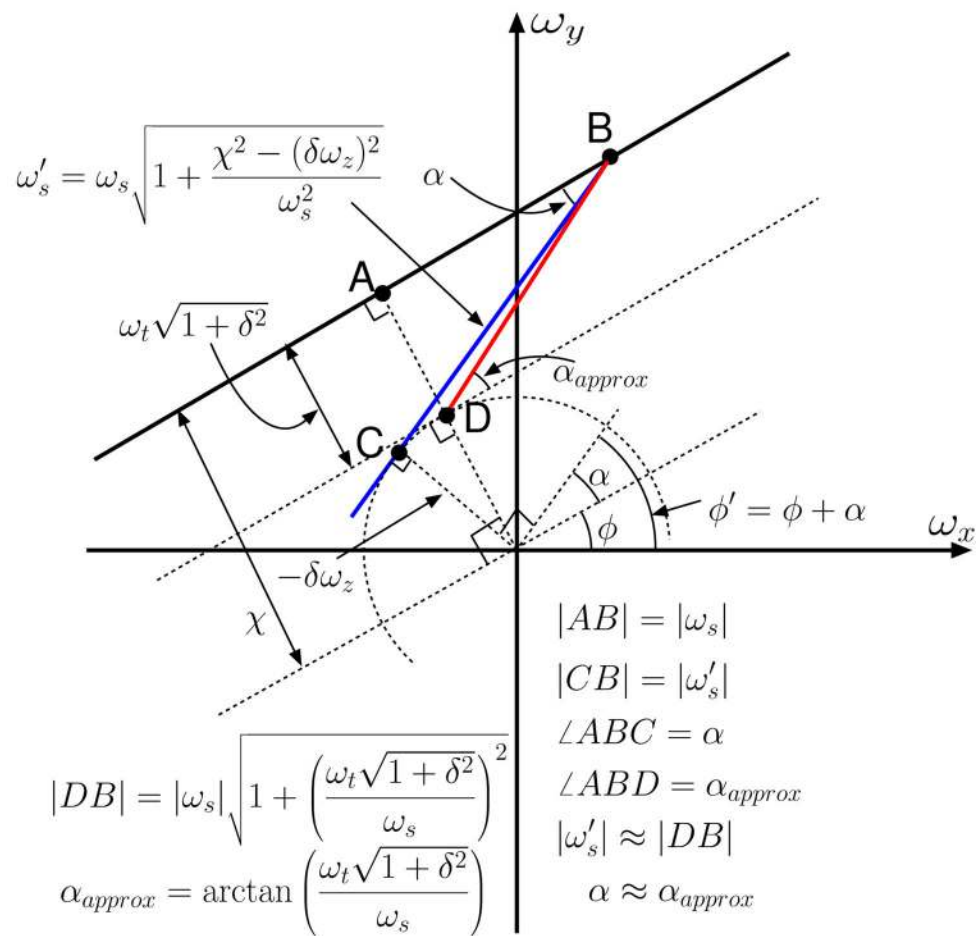
Figure 3.
Graphical interpretation of the exact and approximate inverse Fourier rebinning mappings from 2D non TOF data to 3D non TOF data. Inverse Fourier rebinning is equivalent to finding the coordinates (ω'_s, ϕ') of a point (for example, point *B*) on a trajectory (for example, the line joining the points *A* and *B*) mapped from the 3D sinogram. In the approximate inverse rebinning, |*CB*| and ∠*ABC* are approximated by |*AB*| and $-\delta\omega_z/\omega_s$ respectively.

Figure 4.
Graphical interpretation of the exact and approximate inverse Fourier rebinning mappings from 3D non TOF data to 3D TOF data. The exact inverse Fourier rebinning is equivalent to finding the coordinate information of the line segment CB ($|CB|$ and $\angle ABC$) for the line segment AB. By the approximation in (16), $|CB|$ and $\angle ABC$ are approximated by $|DB|$ and $\angle ABD$, respectively.
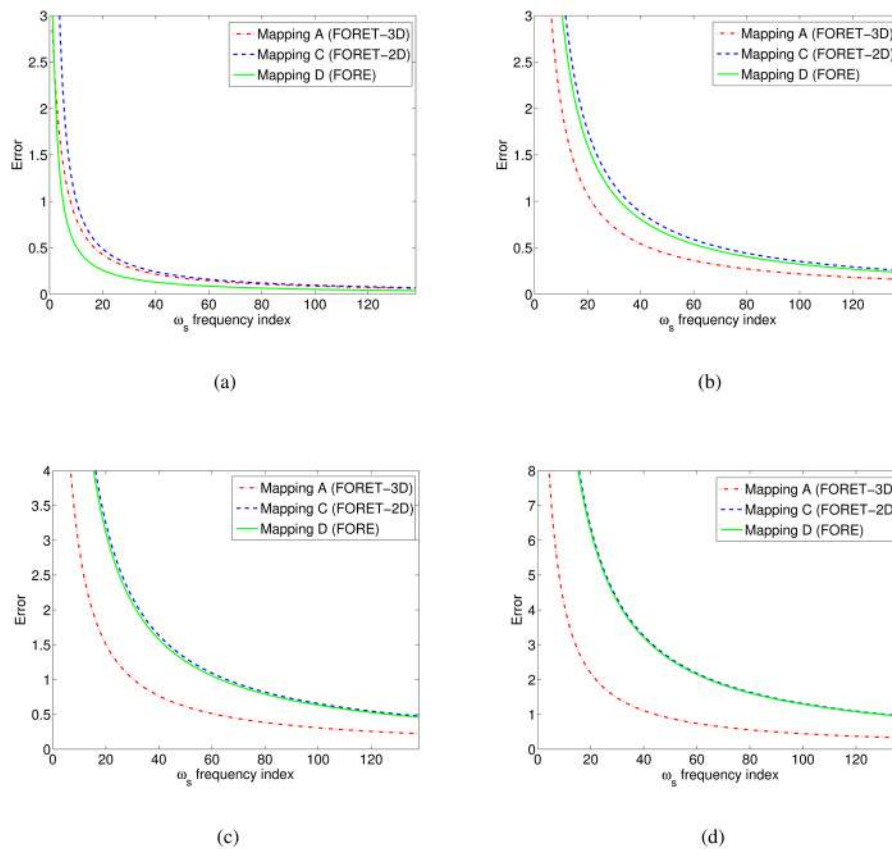
Figure 5.
Averaged mapping errors of approximate rebinnings for different ring differences: (a) Ring difference (RD) = 10 (oblique angle $\theta = 2.7°$), (b) RD = 25 ($\theta = 6.8°$), (c) RD = 35 ($\theta = 9.4°$), (d) RD = 50 ($\theta = 13.4°$). The error value is normalized by the image frequency sample interval ($\Delta\omega_x$) in the transverse plane where $\Delta\omega_x = 1/2/256$ mm^{-1} in our simulation. Notice the error is very large when ω_s is small, so special consideration will be required in this region, similarly to the FORE implementation of (Defrise et al. 1997).
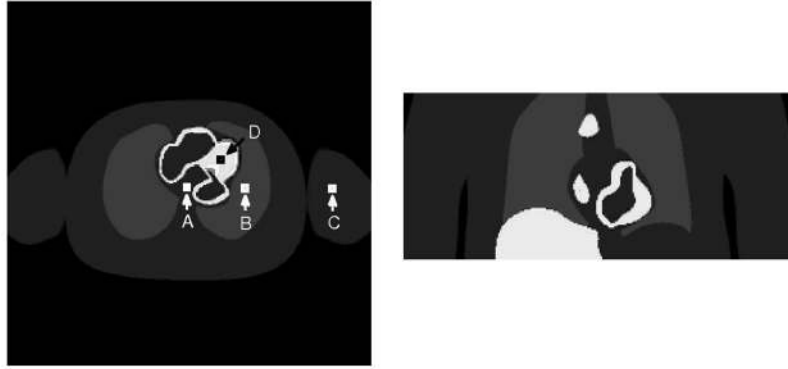
Figure 6.
A transverse and a sagittal plane of the NCAT torso phantom (Segars 2001) used for simulation studies. The resolution and variance of reconstructions were studied at the four points denoted by A, B, C and D.
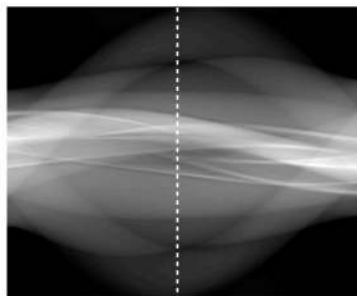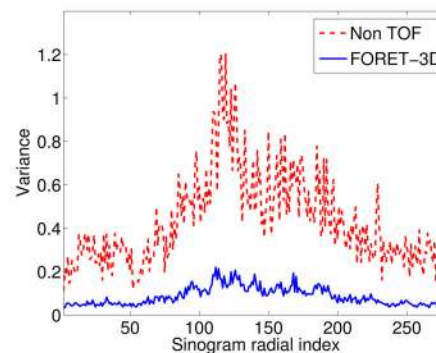
(a)
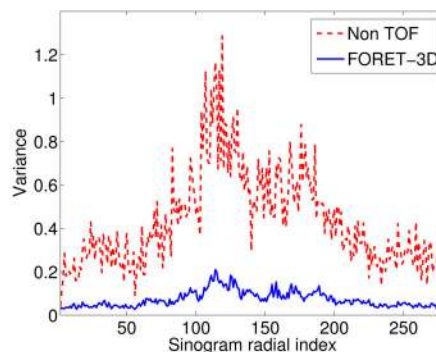
(b)
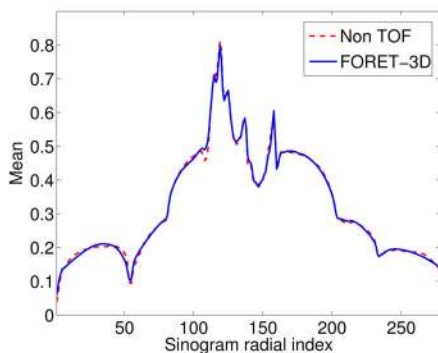
(c)

(d)

Figure 7.
A comparison of the mean and variance of rebinned sinograms, obtained by FORET-3D, and non TOF sinograms for two ring differences: (a) Mean of rebinned sinograms for RD (ring difference) = 0, (b) Variance profiles of rebinned and non TOF sinograms (RD=0), (c) Mean profiles of rebinned and non TOF sinograms (RD=54), (d) Variance profiles of rebinned and non TOF sinograms (RD=54). The profiles were taken at the 160-th angle shown as a dashed line in (a).
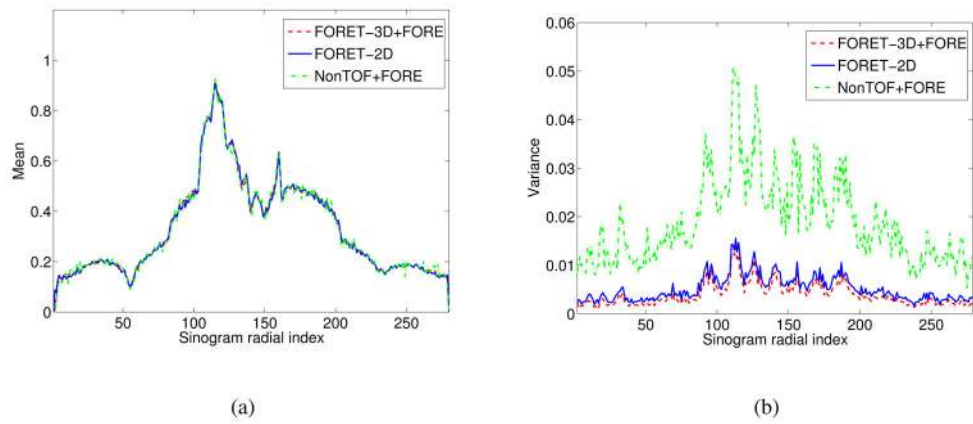
Figure 8.
A comparison of the mean and variance of rebinned direct 2D sinograms obtained by 1) FORET-3D+FORE, 2) FORET-2D and 3) FORE of 3D non TOF data acquired summing the 3D TOF data over the TOF bins: (a) Mean of rebinned sinograms at axial center, (b) Variance of rebinned sinograms at axial center. The profiles were taken at the 160-th angle shown as a dashed line in Figure 7(a).
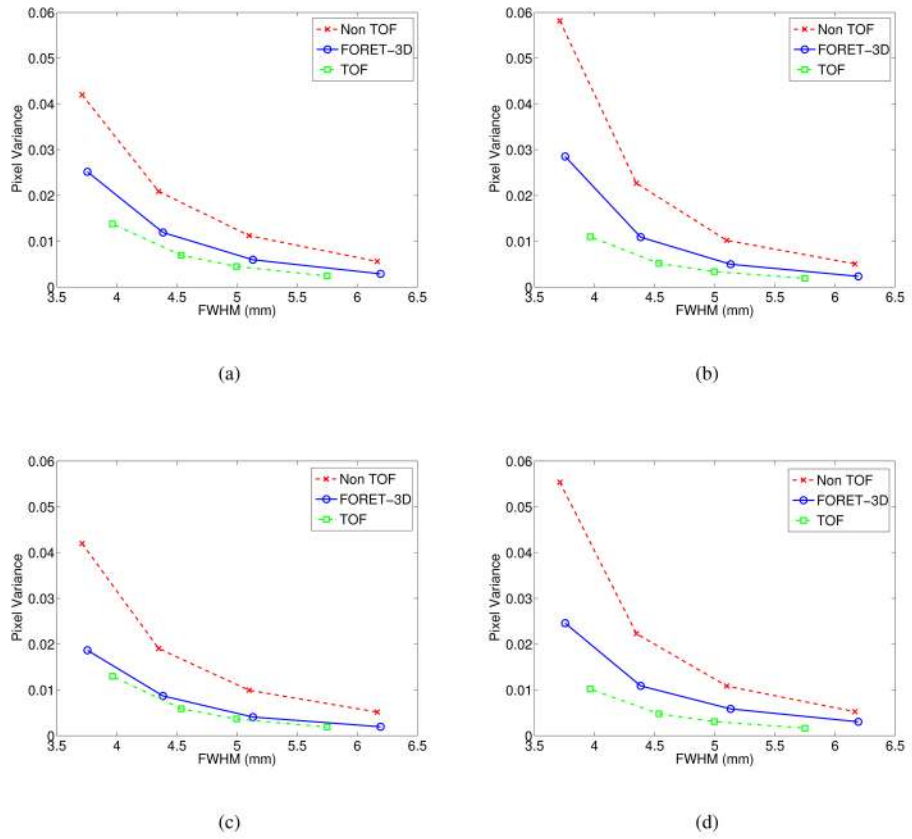
Figure 9.
MC simulation for 2D image reconstruction: Resolution (FWHM) versus pixel variance plot for four different locations. (a) Pixel location A, (b) Pixel location B, (c) Pixel location C, (d) Pixel location D (see Figure 6).
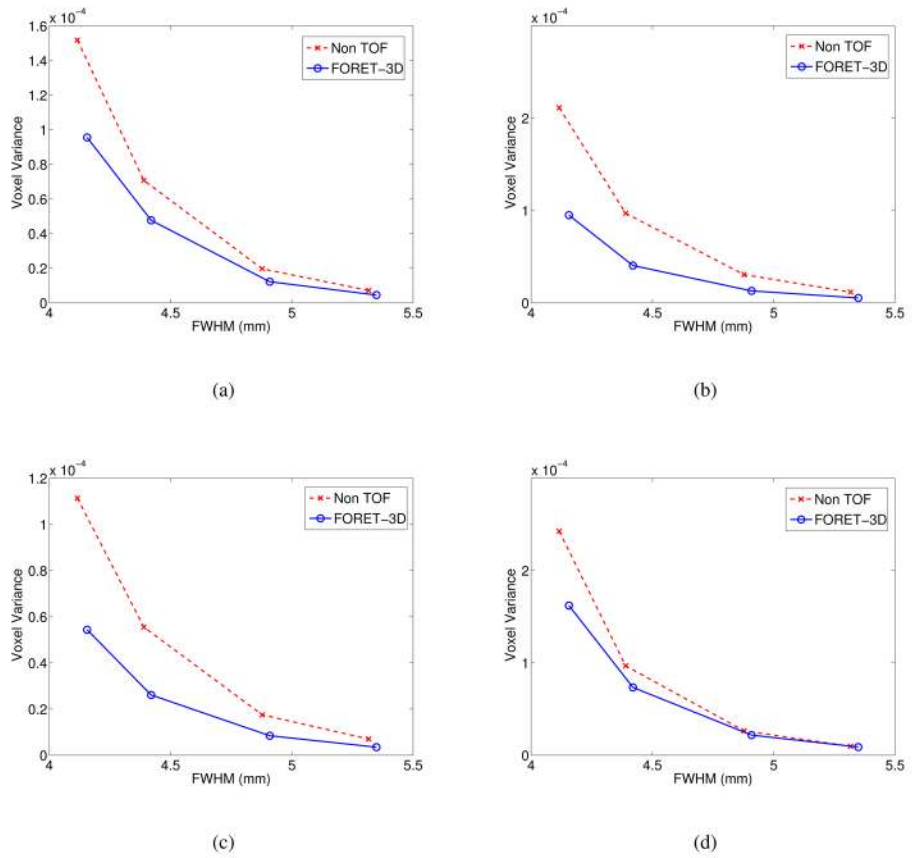
Figure 10.
MC simulation for 3D image reconstruction: Resolution (FWHM) versus voxel variance plot for four different locations in a transverse plane at axial center as shown in Figure 6. (a) Voxel location A, (b) Voxel location B, (c) Voxel location C, (d) Voxel location D.
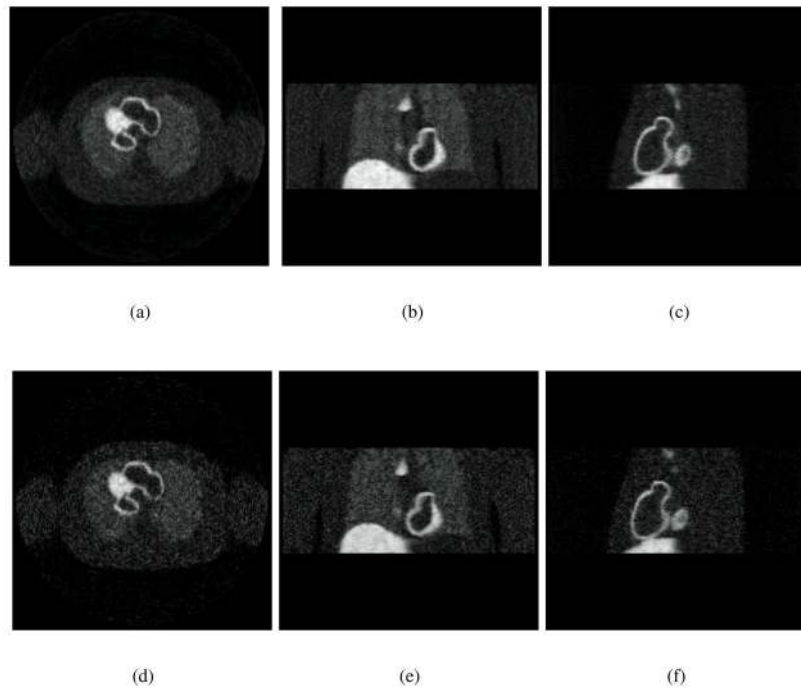
Figure 11.
A comparison of 3D TOF data reconstruction by 'FORET-3D+MAP' (top row) and 'non TOF+MAP' (bottom row) in the transverse view (first column), coronal view (second column) and sagittal view (third column).

Table 1

Rebinning mappings derived from the generalized projection slice theorem

Mapping	Involved data sets	Mapping equations
A	3D TOF data $\wp(\omega_s, \varphi, \omega_z, \delta; \omega_t)$ 3D non TOF data $\wp(\omega_s', \phi', \omega_z, \delta; 0)$	$\omega_x = \omega_s\cos\phi - \chi\sin\phi = \omega_s'\cos\phi' + \delta\omega_z\sin\phi'$ $\omega_y = \omega_s\sin\phi + \chi\cos\phi = \omega_s'\sin\phi' - \delta\omega_z\cos\phi'$
B	3D TOF data $\wp(\omega_s, \varphi, \omega_z, \delta; \omega_t)$ 2D TOF data $\wp(\omega_s', \phi', \omega_z, 0; \omega_t)$	$\omega_x = \omega_s\cos\phi - \chi\sin\phi = \omega_s'\cos\phi' - \omega_t\sin\phi'$ $\omega_y = \omega_s\sin\phi + \chi\cos\phi = \omega_s'\sin\phi' + \omega_t\cos\phi'$
C	3D TOF data $\wp(\omega_s, \varphi, \omega_z, \delta; \omega_t)$ 2D non TOF data $\wp(\omega_s', \phi', \omega_z, 0; 0)$	$\omega_x = \omega_s\cos\phi - \chi\sin\phi = \omega_s'\cos\phi'$ $\omega_y = \omega_s\sin\phi + \chi\cos\phi = \omega_s'\sin\phi'$
D	3D non TOF data $\wp(\omega_s, \varphi, \omega_z, \delta; 0)$ 2D non TOF data $\wp(\omega_s', \phi', \omega_z, 0; 0)$	$\omega_x = \omega_s\cos\phi + \delta\omega_z\sin\phi = \omega_s'\cos\phi'$ $\omega_y = \omega_s\sin\phi - \delta\omega_z\cos\phi = \omega_s'\sin\phi'$
E	2D TOF data $\wp(\omega_s, \varphi, \omega_z, 0; \omega_t)$ 2D non TOF data $\wp(\omega_s', \phi', \omega_z, 0; 0)$	$\omega_x = \omega_s\cos\phi - \omega_t\sin\phi = \omega_s'\cos\phi'$ $\omega_y = \omega_s\sin\phi + \omega_t\cos\phi = \omega_s'\sin\phi'$

Table 2

Exact and approximate points in (ω_x, ω_y) plane for the inverse rebinning for mappings C and A.

	mapping C	mapping A
ω_x^{exact} ω_y^{exact}	$\omega_s' \cos\phi'$ $\omega_s' \sin\phi'$	$\omega_s' \cos\phi' + \delta\omega_z \sin\phi'$ $\omega_s' \sin\phi' - \delta\omega_z \cos\phi'$
ω_x^{approx} ω_y^{approx}	$\tilde{\omega}_s' \cos\tilde{\phi}'$ $\tilde{\omega}_s' \sin\tilde{\phi}'$	$\tilde{\omega}_s' \cos\tilde{\phi}' + \delta\omega_z \sin\tilde{\phi}'$ $\tilde{\omega}_s' \sin\tilde{\phi}' - \delta\omega_z \cos\tilde{\phi}'$

Table 3

Simulated 3D TOF cylindrical PET system parameters

Parameter	Value
Ring radius (mm)	421
Detectors per ring	672
Number of rings	55
Rays (LORs) per angle	336
Maximum ring difference (MRD)	54
Maximum oblique angle θ (degrees)	14.4
Span	11
TOF resolution (ps)	500
Number of TOF bins	13
Image size	$256 \times 256 \times 109$
Transverse voxel size (mm)	2
Scanner axial FOV (mm)	216